# Synthesis and Characterization of Fe(II) β-Diketonato Complexes with Relevance to Acetylacetone Dioxygenase: Insights into the Electronic Properties of the 3-Histidine Facial Triad

Heaweon Park, Jacob S. Baus, Sergey V. Lindeman, and Adam T. Fiedler*

Department of Chemistry, Marquette University, Milwaukee, Wisconsin 53201-1881, United States

Ⓢ Supporting Information

ABSTRACT: A series of high-spin iron(II) β-diketonato complexes have been prepared and characterized with the intent of modeling the substrate-bound form of the enzyme acetylacetone dioxygenase (Dke1). The Dke1 active site features an Fe(II) center coordinated by three histidine residues in a facial geometry—a departure from the standard 2-histidine-1-carboxylate (2H1C) facial triad dominant among nonheme monoiron enzymes. The deprotonated β-diketone substrate binds to the Fe center in a bidentate fashion. To better understand the implications of subtle changes in coordination environment for the electronic structures of nonheme Fe active sites, synthetic models were prepared with three different supporting ligands (L_{N3}): the anionic ^{Me2}Tp and ^{Ph2}Tp ligands (^{R2}Tp = hydrotris(pyrazol-1-yl)borate substituted with R-groups at the 3- and 5-pyrazole positions) and the neutral ^{Ph}TIP ligand (^{Ph}TIP = tris(2-phenylimidazol-4-yl)phosphine). The resulting $[(L_{N3})Fe(acac^X)]^{0/+}$ complexes ($acac^X$ = substituted β-diketonates) were analyzed with a combination of experimental and computational methods, namely, X-ray crystallography, cyclic voltammetry, spectroscopic techniques (UV–vis absorption and ^{1}H NMR), and density functional theory (DFT). X-ray diffraction results for complexes with the ^{Me2}Tp ligand revealed six-coordinate Fe(II) centers with a bound MeCN molecule, while structures of the ^{Ph2}Tp and ^{Ph}TIP complexes generally exhibited five-coordinate geometries. Each $[(L_{N3})Fe(acac^X)]^{0/+}$ complex displays two broad absorption features in the visible region that arise from Fe(II)→$acac^X$ charge transfer and $acac^X$-based transitions, consistent with UV–vis data reported for Dke1. These absorption bands, along with the Fe redox potentials, are highly sensitive to the identity of L_{N3} and substitution of the β-diketonates. By interpreting the experimental results in conjunction with DFT calculations, detailed electronic-structure descriptions of the complexes have been obtained, with implications for our understanding of the Dke1 active site.

[Fe(^{Me2}Tp)(acac)(MeCN)]   [Fe(^{Ph}TIP)(acac)]$^+$
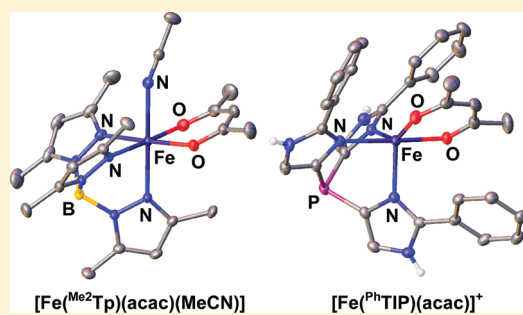
1. INTRODUCTION

The widespread presence of pollutants in the environment remains a major ecological problem and threat to human health. One viable approach for the restoration of contaminated soils and groundwaters utilizes the power of microorganisms to degrade and detoxify pollutants, a process known as bioremediation.[1] The aerobic degradation of pollutants relies heavily on mononuclear nonheme iron dioxygenases found in the catabolic pathways of bacteria.[2] Examples include the Rieske dioxygenases,[3] extradiol catechol dioxygenases,[4] and (chloro)hydroquinone dioxygenases.[5] These enzymes share a common active-site structure in which the Fe(II) center is coordinated to one aspartate (or glutamate) and two histidine residues in a facial array; two or three bound H_2O molecules are also found in the resting states.[6,7] The advantage of this 2-His-1-carboxylate (2H1C) motif is that it permits the Fe center to bind both substrate and O_2 at adjacent coordination sites in an ordered mechanism.[8] The endogenous ligands also play an important role in modulating the electronic structure of the active site, particularly the redox potential of the Fe center.
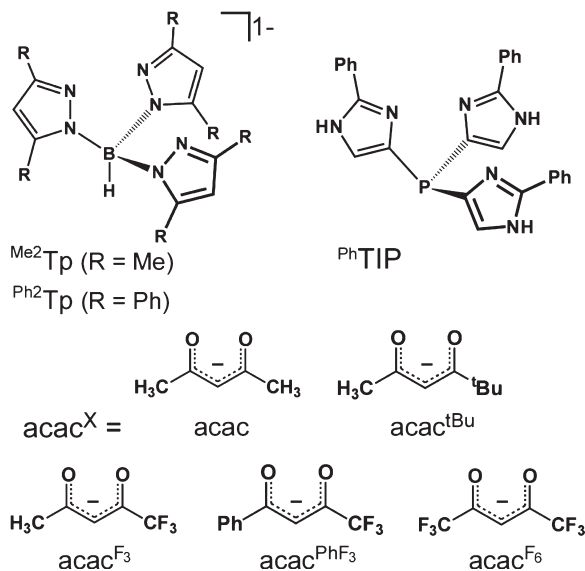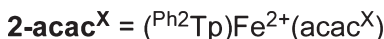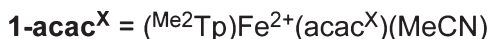
Despite the predominance of the 2H1C motif, a new class of mononuclear nonheme Fe dioxygenases has recently emerged that employ the three histidine (3His) facial triad instead.[9] The first member of this class to be structurally characterized was cysteine dioxygenase (CDO), an enzyme that catalyzes the first step in the catabolism of L-cysteine.[10] Other 3His enzymes have since been discovered in bacteria, where they act to degrade xenobiotic compounds.[11] The enzyme acetylacetone dioxygenase (Dke1), for instance, is one of the few Fe-dependent dioxygenases capable of oxidatively cleaving aliphatic C—C bonds.[12–14] Dke1 allows *Acinetobacter johnsonii* to convert the toxic and prevalent pollutant acetylacetone to acetic acid and 2-oxopropanal. X-ray diffraction (XRD) studies confirmed that the metal center in Dke1 is facially coordinated by three His residues and presumably 2—3 H_2O molecules, although these were not resolved in the structure.[15,16] While the active site can bind several first-row transition metal ions, only Fe(II) results in catalytic activity.[12] Spectroscopic and computational studies indicate that the substrate coordinates to Fe as the deprotonated β-diketone (acac) in a bidentate manner.[14,15]

Scheme 1

1-acac^X = (^{Me2}Tp)Fe^{2+}(acac^X)(MeCN)

2-acac^X = (^{Ph2}Tp)Fe^{2+}(acac^X)

[3-acac^X]OTf = [(^{Ph}TIP)Fe^{2+}(acac^X)](OTf)

^{Me2}Tp (R = Me)
^{Ph2}Tp (R = Ph)

^{Ph}TIP

acac^X =

acac

acac^{tBu}

acac^{F3}

acac^{PhF3}

acac^{F6}

The emergence of the 3His family of Fe dioxygenases raises a pertinent question: what is the significance of variations in Fe coordination environment for the electronic structure and catalytic activity of dioxygenases? Interestingly, a mutant of Dke1 in which the His104 ligand was replaced with Glu was able to partially bind Fe (~30% of wild type) yet exhibited no catalytic activity.[16] Thus, the 2H1C and 3His motifs are not functionally interchangeable, yet it remains unclear exactly how these ligand-sets tune the catalytic properties of their respective enzymes. Another important question concerns the mechanism of oxidative C—C bond cleavage in Dke1. On the basis of kinetic data, Straganz and co-workers have proposed that the mechanism proceeds via concerted addition of O_2 to give an alkylperoxidate intermediate.[14] Such a mechanism would resemble the one proposed for the intradiol catechol dioxygenases in which the role of the Fe center is to activate the substrate, not O_2.[17] Yet a more conventional O_2-activation mechanism has also been suggested that involves initial formation of an Fe-superoxo intermediate, followed by reaction with bound substrate.[15,18]

These fundamental questions concerning the structure and function of Dke1 can be addressed, in part, through the development of synthetic model complexes. Two Fe-acac^X complexes related to the Dke1 active site have been previously reported. Several years prior to the discovery of Dke1, Kitajima et al. published the synthesis and X-ray structure of [(^{iPr2}Tp)Fe(acac)(MeCN)], where ^{iPr2}Tp = hydrotris(3,5-diisopropylpyrazol-1-yl)borate(−1).[19] In 2008, Siewert and Limberg prepared [(^{Me2}Tp)Fe(Phmal)] (Phmal = anion of diethyl phenylmalonate) and demonstrated that reaction with O_2 at room temperature in MeCN resulted in dioxygenolytic ring cleavage of the bound ligand.[18] Thus, both Dke1 models reported to date utilize ^{R2}Tp ligands (Scheme 1), which have been widely employed to replicate the 2H1C facial triad.[7,20,21] However, these pyrazole-based ligands have limitations as mimics of the 3His

facial triad; pyrazole rings have different electronic properties than histidines (i.e., imidazoles), and the overall negative charge of the Tp ligand contrasts with the neutral 3His set of the enzyme. For such reasons, we have also pursued the tris(2-phenylimidazol-4-yl)phosphine ligand (^{Ph}TIP; see Scheme 1) to more faithfully replicate the charge and donor strength of the 3His coordination environment. Related TIP ligands were first developed to model the active sites of Zn-containing carbonic anhydrase and various Cu systems.[22,23] Iron complexes with these trisimidazole ligands are relatively rare, though, with all such examples involving homoleptic [Fe(TIP)$_2$]$^{2+/3+}$ complexes[24,25] or carboxylate-bridged multinuclear species.[25,26]

In an effort to better understand the significance of the 3His triad for Dke1, we have synthesized a series of Fe(II)-acac^X complexes featuring the three supporting ligands (L_{N3}) shown in Scheme 1: ^{Me2}Tp, ^{Ph2}Tp, and ^{Ph}TIP. As noted above, the ^{R2}Tp and ^{Ph}TIP ligands each reproduce the facial N3 coordination environment of the Dke1 active site, yet they have important differences with respect to charge and electronic properties that resemble those differences between the 2H1C and 3His triads. Since a previous study by Solomon and co-workers suggested that the acac-bound Dke1 site partially retains a bound H_2O ligand,[27] we employed both ^{Me2}Tp and ^{Ph2}Tp ligands to generate six-coordinate (6C) and five-coordinate (5C) complexes, respectively. In addition to the natural Dke1 substrate (acac), our models were prepared with acac^X ligands featuring bulky and/or electron-withdrawing substituents (Scheme 1) to evaluate the effect such variations on the structural and spectroscopic features of the resulting complexes. Each complex was characterized with X-ray crystallography, cyclic voltammetry, and electronic absorption and ^{1}H NMR spectroscopies. Density functional theory (DFT) calculations were also performed to examine the effects of ligand charge and coordination number on Fe/ligand bonding interactions. This combined experimental and computational approach has provided detailed insights into the electronic structures of the synthetic Fe(II)-acac^X complexes and, by extension, the Dke1 active site.

2. EXPERIMENTAL SECTION

Materials. All reagents and solvents were purchased from commercial sources and used as received unless otherwise noted. Acetonitrile (MeCN), dichloromethane, and tetrahydrofuran (THF) were purified and dried using a Vacuum Atmospheres solvent purification system. The L_{N3} supporting ligands K(^{Me2}Tp),[28] K(^{Ph2}Tp),[29] and ^{Ph}TIP[23] were prepared according to literature procedures. The synthesis and handling of air-sensitive materials were carried out under inert atmosphere using a Vacuum Atmospheres Omni-Lab glovebox equipped with a freezer set to −30 °C.

Physical Methods. Elemental analyses were performed at Midwest Microlab, LLC, in Indianapolis, IN. Infrared (IR) spectra of the Fe-acac^X complexes were measured as KBr pellets using a Nicolet Magna-IR 560 spectrometer. ^{1}H and ^{19}F NMR spectra were collected at room temperature with a Varian 400 MHz spectrometer; ^{19}F NMR spectra were referenced using the benzotrifluoride peak at −63.7 ppm. UV−vis spectra were obtained with an Agilent 8453 diode array spectrometer. Electrochemical measurements were performed with an epsilon EC potentiostat (iBAS) under nitrogen atmosphere at a scan rate of 100 mV/s with 60 mM (NBu$_4$)PF$_6$. A three-electrode cell containing a Ag/AgCl reference electrode, a platinum auxiliary electrode, and a glassy carbon working electrode was employed for cyclic voltammetric (CV) measurements. Under these conditions, the ferrocene/ferrocenium

($Fc^{+/0}$) couple has an $E_{1/2}$ value of +474 mV in MeCN and 1:1 MeCN:CH_2Cl_2 solutions.

General Procedure for Synthesis of (^{R2}Tp)Fe(acac^X) Complexes (R = Me, Ph). These complexes were generated using a modified version of the procedure reported by Siewert et al.[18] The Na(acac^X) salts were prepared by mixing the appropriate β-diketone (1.0 mmol) with NaOMe (1.0 mmol) in THF for 30 min. Afterward, the solvent was removed under vacuum to yield the Na(acac^X) salt as a white solid. Anhydrous $FeCl_2$ (1.0 mmol), $K^{R2}Tp$ (1.0 mmol), and 10 mL of MeCN were then added to the flask, and the reaction mixture was stirred overnight at ambient temperature. The solution was filtered to remove inorganic salts (NaCl and KCl) and any Fe(^{R2}Tp)$_2$ byproduct, and the volume of the resulting solution was reduced by half. For the Fe(^{Me2}Tp)(acac^X) complexes, storage of this solution (with a concentration of ∼0.2 M) at −30 °C yielded crystals suitable for X-ray diffraction analysis. The crystallization methods used for the Fe(^{Ph2}Tp)-(acac^X) complexes are described below for each complex.

(^{Me2}Tp)Fe(acac). Yield: 114 mg, 25%. Anal. Calcd for $C_{20}H_{29}BFeN_6O_2$: C, 53.13; H, 6.46; N, 18.59. Found: C, 53.03; H, 6.28; N, 18.57. UV−vis [λ_{max}, nm (ε, M^{-1} cm^{-1}) in MeCN]: 438 (620), 348 (630). IR (KBr, cm^{-1}): 2955, 2922, 2520 [ν(BH)], 1590 [ν(CO)], 1450, 1400, 1200.

(^{Me2}Tp)Fe(acac^{F3}). Yield: 46 mg, 11%. Anal. Calcd for $C_{20}H_{26}BF_3FeN_6O_2$: C, 47.46; H, 5.18; N, 16.61. Found: C, 47.65; H, 5.15; N, 16.39. UV−vis [λ_{max}, nm (ε, M^{-1} cm^{-1}) in MeCN]: 479 (580), 377 (400). IR (KBr, cm^{-1}): 2962, 2928, 2534 [ν(BH)], 1616 [ν(CO)], 1543, 1450, 1292, 1188, 1138 (CF$_3$). ^{19}F NMR (CD$_3$CN): −56.2.

(^{Me2}Tp)Fe(acac^{PhF3}). Yield: 352 mg, 62%. Anal. Calcd for $C_{25}H_{28}BF_3FeN_6O_2$: C, 52.85; H, 4.97; N, 14.79. Found: C, 53.03; H, 5.03; N 14.72. UV−vis [λ_{max}, nm (ε, M^{-1} cm^{-1}) in MeCN]: 567 (1190), 403 (570). IR (KBr, cm^{-1}): 2962, 2931, 2526 [ν(BH)], 1604 [ν(CO)], 1573, 1537, 1450, 1288, 1196, 1142 (CF$_3$). ^{19}F NMR (CD$_3$CN): −64.6.

(^{Me2}Tp)Fe(acac^{F6}). Yield: 206 mg, 48%. Anal. Calcd for $C_{20}H_{23}BF_6FeN_6O_2$: C, 42.89; H, 4.14; N, 15.00. Found: C 42.97, H 4.22, N 15.22. UV−vis [λ_{max}, nm (ε, M^{-1} cm^{-1}) in MeCN]: 571 (820), 398 (560). IR (KBr, cm^{-1}): 2966, 2928, 2530 [ν(BH)], 1628 [ν(CO)], 1543, 1450, 1254, 1196, 1142 (CF$_3$). ^{19}F NMR (CD$_3$CN): −78.9.

(^{Ph2}Tp)Fe(acac). Slow evaporation of a MeCN solution provided yellow-green crystals after several days. Yield: 172 mg, 21%. Anal. Calcd for $C_{50}H_{41}BFeN_6O_2$: C, 72.83; H, 5.01; N, 10.19. Found: C, 71.69; H, 5.03; N, 10.02. UV−vis [λ_{max}, nm (ε, M^{-1} cm^{-1}) in MeCN]: 420 (410), 356 (sh). IR (KBr, cm^{-1}): 3059, 2611 [ν(BH)], 1585 [ν(CO)], 1477, 1362.

(^{Ph2}Tp)Fe(acac^{tBu}). All MeCN was removed under vacuum, and the yellow solid was redissolved in 5 mL of THF and filtered. Layering the filtrate with MeCN provided yellow crystals suitable for X-ray diffraction. Yield: 199 mg, 23%. Anal. Calcd for $C_{53}H_{47}BFeN_6O_2$: C, 73.25; H, 5.47; N, 9.70. Found: C, 72.85; H, 5.46; N, 9.39. UV−vis [λ_{max}, nm (ε, M^{-1} cm^{-1}) in MeCN]: 424 (420), 361 (sh). IR (KBr, cm^{-1}): 3062, 2615 [ν(BH)], 1583 [ν(CO)], 1479, 1362, 1169.

(^{Ph2}Tp)Fe(acac^{F3}). All MeCN was removed under vacuum, and the orange solid was redissolved in 5 mL of CH_2Cl_2 and filtered. Layering the filtrate with MeCN provided reddish orange crystals suitable for X-ray diffraction. Yield: 194 mg, 22%. Anal. Calcd for $C_{50}H_{38}BF_3FeN_6O_2$: C, 68.36; H, 4.36; N, 9.57. Found: C, 68.63; H, 4.51; N, 9.71. UV−vis [λ_{max}, nm (ε, M^{-1} cm^{-1}) in MeCN]: 462 (440), 363 (sh). IR (KBr, cm^{-1}): 3060, 2620 [ν(BH)], 1630 [ν(CO)], 1480, 1360, 1170, 1140 (CF$_3$). ^{19}F NMR (C$_6$D$_6$): −46.6.

(^{Ph2}Tp)Fe(acac^{PhF3}). All MeCN was removed under vacuum, and the purple solid was redissolved in 5 mL of CH_2Cl_2 and filtered. Layering the filtrate with MeCN provided reddish purple crystals suitable for X-ray diffraction. Yield: 239 mg, 25%. Anal. Calcd for $C_{55}H_{40}BF_3FeN_6O_2$: C, 70.23; H, 4.29; N, 8.93. Found: C, 69.83; H, 4.29; N, 8.90. UV−vis [λ_{max}, nm (ε, M^{-1} cm^{-1}) in MeCN]: 540 (980), 415 (460).

IR (KBr, cm^{-1}): 3062, 2619 [ν(BH)], 1606 [ν(CO)], 1479, 1362, 1169, 1144 (CF$_3$). ^{19}F NMR (C$_6$D$_6$): −42.1.

General Procedure for Synthesis of [(^{Ph}TIP)Fe(acac^X)]OTf Complexes. The appropriate acac^X ligand (1.0 mmol) was stirred with NaOMe (1.0 mmol) in THF for 30 min, after which the solvent was removed under vacuum to yield the Na(acac^X) salt. The ^{Ph}TIP ligand (1.0 mmol) and anhydrous Fe(OTf)$_2$ (1.0 mmol) were each dissolved in 3 mL of MeOH and added dropwise to a flask containing the Na(acac^X) salt in 5 mL of MeOH. The reaction mixture was stirred overnight at ambient temperature, and the solvent was removed by vacuum. The method used to obtain crystals of each ^{Ph}TIP-containing complex is described below.

[(^{Ph}TIP)Fe(acac)]OTf. The solid obtained after removal of the MeOH solvent was dissolved in 5 mL of MeCN. After filtration to remove insoluble materials, the 0.2 M solution was cooled to −30 °C, and yellow crystals formed after several days. Yield: 36%. Anal. Calcd for $C_{33}H_{28}F_3FeN_6O_5PS$: C, 51.84; H, 3.69; N, 10.99. Found: C, 51.52; H, 3.65; N, 10.68. UV−vis [λ_{max}, nm (ε, M^{-1} cm^{-1}) in MeCN]: 415 (160), 351 (sh). IR (KBr, cm^{-1}): 3207, 1587 [ν(CO)], 1559, 1516, 1478, 1458, 1389. ^{19}F NMR (CD$_3$CN): −79.8 (OTf).

[(^{Ph}TIP)Fe(acac^{F3})]OTf. The solid obtained after removal of the MeOH solvent was dissolved in 5 mL of CH_2Cl_2. After filtration, the solution was layered with pentane, providing orange crystals. Anal. Calcd for $C_{33}H_{25}F_6FeN_6O_5PS$: C, 48.43; H, 3.08; N, 10.27. Found: C, 48.05; H, 3.24; N, 10.04. UV−vis [λ_{max}, nm (ε, M^{-1} cm^{-1}) in MeCN]: 461 (220), 373 (sh). IR (KBr, cm^{-1}): 3221, 1630 [ν(CO)], 1559, 1478, 1458. ^{19}F NMR (CD$_3$CN): −45.1 (acac^{F3}), −79.8 (OTf).

[(^{Ph}TIP)Fe(acac^{PhF3})]OTf. The solid obtained after removal of the MeOH solvent was dissolved in 5 mL of CH_2Cl_2. The solution was filtered and then layered with pentane, yielding reddish crystals. Anal. Calcd for $C_{38}H_{27}F_6FeN_6O_5PS$: C, 51.83; H, 3.09; N, 9.54. Found: C, 50.30; H, 3.18; N, 9.13 (the slight discrepancy in the carbon value indicates that small amounts of impurities are present). UV−vis [λ_{max}, nm (ε, M^{-1} cm^{-1}) in MeCN]: 528 (630), 408 (320). IR (KBr, cm^{-1}): 3223, 1609 [ν(CO), 1574, 1478, 1457. ^{19}F NMR (CD$_3$CN): −48.3 (acac^{PhF3}), −79.8 (OTf).

[(^{Ph}TIP)Fe(acac^{F6})]OTf. The solid obtained after removal of the MeOH solvent was dissolved in 5 mL of CH_2Cl_2, filtered to remove insoluble materials, and then layered with pentane to give purple crystals. Yield: 25%. Anal. Calcd for $C_{33}H_{22}F_9FeN_6O_5PS$: C, 45.43; H, 2.54; N, 9.63. Found: C, 43.19; H, 2.80; N, 9.32 (the minor discrepancies indicate that small amounts of impurities are present). UV−vis [λ_{max}, nm (ε, M^{-1} cm^{-1}) in MeCN]: 509 (450), 381 (390). IR (KBr, cm^{-1}): 3206, 1632 [ν(CO)], 1560, 1480. ^{19}F NMR (CD$_3$CN): −63.1 (acac^{F6}), −79.8 (OTf).

Crystallographic Studies. The 12 newly synthesized complexes reported here were each characterized using X-ray crystallography. The X-ray diffraction data were collected at 100 K with an Oxford Diffraction SuperNova kappa-diffractometer equipped with dual microfocus Cu/Mo X-ray sources, X-ray mirror optics, Atlas CCD detector and a low-temperature Cryojet device. Crystallographic data for the compounds are provided in Table 1. The data were processed with CrysAlisPro program package (Oxford Diffraction Ltd., 2010) typically using a numerical Gaussian absorption correction (based on the real shape of the crystal) followed by an empirical multiscan correction using the SCALE3 ABSPACK routine. The structures were solved using the SHELXS program and refined with the SHELXL program[30] within the Olex2 crystallographic package.[31] All computations were performed on an Intel PC computer with Windows 7 OS. The majority of the structures contain a certain degree of disorder that was detected in difference Fourier syntheses of electron density and accounted for using capabilities of the SHELX package. In most cases, hydrogen atoms were localized in difference syntheses of electron density but were refined using appropriate geometric restrictions on the corresponding bond lengths and bond angles within a riding/rotating model (torsion angles

11980

dx.doi.org/10.1021/ic201115s |*Inorg. Chem.* 2011, 50, 11978–11989

Table 1. Summary of X-ray Crystallographic Data Collection and Structure Refinement

	1-acac·2MeCN	1-acac^{F3}·MeCN	1-acac^{PhF3}·MeCN	1-acac^{F6}	2-acac	2-acac^{tBu}·0.5THF·0.5 MeCN
empirical formula	$C_{26}H_{38}BFeN_9O_2$	$C_{24}H_{32}BF_3FeN_8O_2$	$C_{29}H_{34}BF_3FeN_8O_2$	$C_{22}H_{26}BF_6FeN_7O_2$	$C_{50}H_{41}BFeN_6O_2$	$C_{56}H_{52.5}BFeN_{6.5}O_{2.5}$
formula weight	575.31	588.24	650.30	601.16	824.55	923.20
crystal system	triclinic	monoclinic	monoclinic	monoclinic	monoclinic	monoclinic
space group	$P\bar{1}$	$P2_1/n$	$P2_1/c$	$P2_1/n$	$P2_1/n$	$P2_1/n$
a, Å	7.8894(2)	11.32026(9)	16.3762(7)	11.72084(10)	13.88320(12)	9.75151(12)
b, Å	12.1386(3)	19.30082(13)	12.3527(9)	19.56928(16)	18.87572(15)	35.2674(4)
c, Å	16.3511(4)	13.78973(11)	16.0614(6)	11.95953(9)	16.93576(18)	13.67554(17)
α, deg	91.901(2)	90	90	90	90	90
β, deg	98.880(2)	106.1061(8)	102.273(5)	99.6456(8)	112.1370(11)	94.0112(11)
γ, deg	97.026(2)	90	90	90	90	90
V, Å^3	1533.33(7)	2894.66(4)	3174.8(3)	2704.36(4)	4110.95(7)	4691.63(10)
Z	2	4	4	4	4	4
D_{calc}, g/cm^3	1.246	1.350	1.361	1.477	1.332	1.307
λ, Å	0.7107	1.5418	1.5418	0.7107	0.7107	1.5418
μ, mm^{-1}	0.53	4.658	4.303	0.633	0.416	2.984
θ-range, deg	3 to 33	4 to 77	5 to 74	3 to 38	3 to 33	3 to 71
reflections collected	71038	27495	13228	81670	59544	22809
independent reflections	10798	6018	6281	14031	14181	8776
	[R_{int} = 0.0537]	[R_{int} = 0.0263]	[R_{int} = 0.0229]	[R_{int} = 0.0247]	[R_{int} = 0.0268]	[R_{int} = 0.0406]
data/restraints/parameters	10789/3/374	6018/24/402	6281/0/405	14031/6/386	14181/0/543	8776/13/645
GOF (on F^2)	1.010	1.010	1.034	1.039	1.085	0.837
R1/wR2 ($I > 2\sigma(I)$) [a]	0.0344/0.0878	0.0288/0.0710	0.0331/0.0818	0.0309/0.0957	0.0352/0.1023	0.0335/0.0673
R1/wR2 (all data)	0.0474/0.0914	0.0327/0.0728	0.0372/0.0853	0.0406/0.0982	0.0502/0.1054	0.0547/0.0710

	2-acac^{F3}·CH$_2$Cl$_2$[b]	2-acac^{PhF3}·CH$_2$Cl$_2$	[3-acac]OTf·MeCN	[3-acac^{F3}]OTf·CH$_2$Cl$_2$	[3-acac^{PhF3}]OTf·4CH$_2$Cl$_2$	[3-acac^{F6}(MeCN)]OTf·2MeCN
empirical formula	$C_{50.87}H_{39.73}BCl_{1.73}F_3FeN_6O_2$	$C_{56}H_{42}BCl_2F_3FeN_6O_2$	$C_{35}H_{31}F_3FeN_7O_5PS$	$C_{34}H_{27}Cl_2F_6FeN_6O_5PS$	$C_{42}H_{35}Cl_8F_6FeN_6O_5PS$	$C_{39}H_{31}F_9FeN_9O_5PS$
formula weight	952.17	1025.52	805.55	903.40	1220.24	995.61
crystal system	monoclinic	monoclinic	triclinic	triclinic	triclinic	orthorhombic
space group	$P2_1/n$	$P2_1/n$	$P\bar{1}$	$P\bar{1}$	$P\bar{1}$	$Pna2_1$
a, Å	9.9620(3)	9.9045(7)	10.8489(3)	10.9737(3)	11.4327(3)	20.3397(3)
b, Å	33.2844(10)	35.733(2)	12.6264(3)	12.6383(3)	12.8330(2)	11.83101(16)
c, Å	13.5814(4)	13.4769(9)	14.4290(4)	14.6113(3)	17.9561(3)	17.8160(2)
α, deg	90	90	87.443(2)	85.8018(19)	85.0393(15)	90
β, deg	94.637(3)	92.429(7)	71.223(2)	71.277(2)	78.0672(17)	90
γ, deg	90	90	89.004(2)	87.183(2)	83.3042(17)	90
V, Å^3	4488.6(2)	4765.4(5)	1869.46(8)	1913.32(8)	2554.66(9)	4287.23(10)
Z	4	4	2	2	2	4
D_{calc}, g/cm^3	1.409	1.429	1.431	1.568	1.586	1.542
λ, Å	1.5418	1.5418	0.7107	0.7107	1.5418	0.7107
μ, mm^{-1}	4.153	4.090	0.568	0.709	7.525	0.532
θ-range, deg	3 to 71	4 to 75	2 to 29	2 to 29	2 to 74	3 to 29
reflections collected	25772	26605	42236	86437	23048	41132
independent reflections	8377	9427	9554	10144	10023	10734
	[R_{int} = 0.2268]	[R_{int} = 0.0545]	[R_{int} = 0.0335]	[R_{int} = 0.0498]	[R_{int} = 0.0542]	[R_{int} = 0.0251]
data/restraints/parameters	8377/0/597	9427/0/640	9554/0/481	10144/26/584	10023/0/631	10734/1/590
GOF (on F^2)	1.063	1.058	1.041	1.081	1.033	1.057
R1/wR2 ($I > 2\sigma(I)$) [a]	0.0804/0.1983	0.0661/0.1452	0.0356/0.0797	0.0361/0.0998	0.0630/0.1744	0.0247/0.0581
R1/wR2 (all data)	0.1107/0.2217	0.0895/0.1553	0.0486/0.0868	0.0477/0.1036	0.0671/0.1810	0.0292/0.0589

[a] $R1 = \Sigma||F_o| - |F_c||/\Sigma|F_o|$; $wR2 = [\Sigma w(F_o^2 - F_c^2)^2/\Sigma w(F_o^2)^2]^{1/2}$. [b] The solvate molecule in 2-acac^{F3}·CH$_2$Cl$_2$ is only partially (87%) populated.

of methyl hydrogens were optimized to better fit the residual electron density).

Density Functional Theory (DFT) Calculations. DFT calculations were performed using the ORCA 2.7 software package
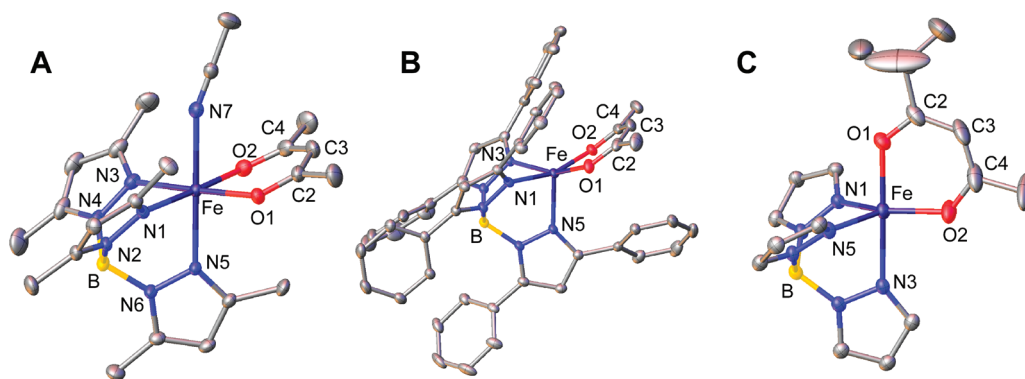
11981

dx.doi.org/10.1021/ic201115s |Inorg. Chem. 2011, 50, 11978–11989

Figure 1. Thermal ellipsoid plots (50% probability) derived from **1-acac**·2MeCN (A), **2-acac** (B), and **2-acac^{tBu}**·0.5MeCN·0.5MeCN (C). Hydrogen atoms and noncoordinating solvent molecules have been omitted for clarity, as well as the Ph-rings at the 3- and 5-positions of the ^{Ph2}Tp ligand in **2-acac^{tBu}**.

developed by Dr. F. Neese.[32] In each case, the corresponding X-ray structure provided the starting point for geometry optimizations and the computational model included the entire complex (excluding counteranions and uncoordinated solvent molecules). Geometry optimizations employed the Becke−Perdew (BP86) functional[33] and Ahlrichs' valence triple-ζ basis set (TZV) for all atoms, in conjunction with the TZV/J auxiliary basis set.[34] Extra polarization functions were used on non-hydrogen atoms. Single-point (SP) calculations involving the optimized models were carried out with Becke's three-parameter hybrid functional for exchange along with the Lee−Yang−Parr correlation functional (B3LYP).[35] These SP calculations also utilized the TZV basis set noted above, but additional polarization functions were included for all atoms, including hydrogens. The same enlarged basis set was used for time-dependent DFT (TD-DFT) calculations,[36] which computed absorption energies and intensities within the Tamm−Dancoff approximation.[37] In each case, at least 20 excited states were calculated. Finally, the gOpenMol program[38] developed by Laaksonen was used to generate isosurface plots of molecular orbitals.

3. RESULTS AND ANALYSIS

A. Synthesis and Solid State Structures. Mononuclear Fe(II) β-diketonato complexes with the ^{Me2}Tp and ^{Ph2}Tp ligands (**1-acac^X** and **2-acac^X**, respectively; Scheme 1) were prepared by mixing 1 equiv of the sodium salt of the appropriate β-diketone, Na(acac^X), with equimolar amounts of FeCl$_2$ and K(^{R2}Tp) in MeCN. The analogous ^{Ph}TIP-containing complexes [**3-acac^X**]OTf were generated via addition of the ligand to MeOH solutions of Na(acac^X) and Fe(OTf)$_2$. All syntheses were performed under anaerobic conditions. Each complex was characterized with single-crystal X-ray crystallography; details concerning the data collection and analysis are summarized in Table 1. While the majority of these complexes crystallize as solvates, elemental analysis indicates that no solvent is present in ground vacuum-dried crystals.

Upon cooling to −30 °C in MeCN, concentrated solutions of **1-acac^X** (acac^X = acac, acac^{F3}, acac^{F6}, and acac^{PhF3}) provided crystals suitable for X-ray diffraction studies. Each of the resulting structures revealed a 6C monoiron(II) center with a facially coordinating ^{Me2}Tp ligand, bidentate acac^X ligand, and bound MeCN. In some cases, the crystals contained one or two equivalents of noncoordinating MeCN. Figure 1A displays the molecular structure of **1-acac**, and selected bond distances and angles for the four **1-acac^X** complexes are provided in Table 2.[39]

Table 2. Selected Metric Parameters for 1-acac·2MeCN, 1-acac^{F3}·MeCN, 1-acac^{PhF3}·MeCN, and 1-acac^{F6} ^{a}

	1-acac· 2MeCN	1-acac^{F3}· MeCN	1-acac^{PhF3}· MeCN	1-acac^{F6}
Fe−O1	2.0882(8)	2.0563(10)	2.0644(11)	2.1116(6)
Fe−O2	2.0510(8)	2.0843(10)	2.0730(11)	2.0976(6)
Fe−N1	2.1535(9)	2.1798(12)	2.1436(13)	2.1502(7)
Fe−N3	2.1851(9)	2.1353(11)	2.1635(13)	2.1154(7)
Fe−N5	2.1748(9)	2.2141(11)	2.1695(13)	2.1461(7)
Fe−N7	2.2363(10)	2.2212(12)	2.2550(14)	2.2461(7)
Fe−O$_{acac}$ (ave)	2.070	2.070	2.069	2.105
Fe−N$_{Tp}$ (ave)	2.171	2.176	2.158	2.137
Fe−N7−CX^b	159.30(9)	161.20(12)	171.49(14)	169.23(7)
acac^X tilt^c	20.0	10.7	18.4	24.4

^{a} Bond distances in Å and angles in deg. ^{b} N7 and CX are atoms in the coordinated MeCN ligand. ^{c} acac^X tilt = average angle between the plane of the acac ligand and a plane defined by the O1−Fe−O2 atoms.

The iron-pyrazole bond lengths (average Fe−N$_{Tp}$ = 2.16 Å) are similar to those observed for other six-coordinate high-spin Fe(II) complexes with Tp ligands.[19,40] The Fe−O$_{acac}$ bond distances vary slightly across the series, with the average value ranging from 2.070 Å for **1-acac** to 2.105 Å for **1-acac^{F6}**. The acac ligands are tilted out of the equatorial N$_2$O$_2$ plane by an average of 18° because of steric interactions with the 3-Me group of the axial pyrazole moiety. The MeCN ligands exhibit Fe−N$_{MeCN}$ bond distances near 2.24 Å and exist in bent conformations with Fe−N−C angles between 159 and 172°.

Complexes with the ^{Ph2}Tp ligand (**2-acac^X**; acac^X = acac, acac^{tBu}, acac^{F3}, and acac^{PhF3}) were crystallized using various methods: slow evaporation of a concentrated MeCN solution (**2-acac**) and diffusion of MeCN into solutions of CH$_2$Cl$_2$ (**2-acac^{F3}** and **2-acac^{PhF3}**) or THF (**2-acac^{tBu}**). In each case, the resulting structures revealed 5C Fe(II) centers lacking bound solvent, even though all crystallizations involved MeCN. As illustrated in the structure of **2-acac** (Figure 1B), two phenyl rings from the ^{Ph2}Tp ligand are positioned over the vacant coordination site, apparently restricting access of solvent to the metal center. The Fe-ligand bond lengths (Table 3) are typical for high-spin Fe(II) complexes, although somewhat shorter than those found in the ^{Me2}Tp structures because of the decrease in

Table 3. Selected Bond Distances (Å) and Bond Angles (deg) for 2-acac, 2-acac^{tBu}·0.5MeCN·0.5THF, 2-acac^{F3}, and 2-acac^{PhF3}·CH$_2$Cl$_2$

	2-acac	2-acac^{tBu}·0.5MeCN· 0.5THF	2-acac^{F3}· CH$_2$Cl$_2$	2-acac^{PhF3}· CH$_2$Cl$_2$
Fe−O1	1.9945(10)	2.0492(13)	2.050(3)	2.054(3)
Fe−O2	2.0239(9)	1.9443(14)	1.986(3)	1.967(3)
Fe−N1	2.1625(10)	2.0945(14)	2.096(3)	2.092(3)
Fe−N3	2.1462(11)	2.2603(15)	2.178(3)	2.231(3)
Fe−N5	2.0984(9)	2.1074(14)	2.117(3)	2.095(3)
Fe−O$_{acac}$ (ave)	2.009	1.997	2.018	2.011
Fe−N$_{Tp}$ (ave)	2.136	2.154	2.130	2.139
O1−Fe−O2	88.82(4)	88.14(6)	86.40(12)	87.21(11)
O1−Fe−N1	91.24(4)	94.55(6)	94.81(12)	95.95(11)
O1−Fe−N3	158.66(4)	177.39(5)	172.58(11)	177.69(11)
O1−Fe−N5	110.44(4)	94.64(5)	97.33(12)	95.34(11)
O2−Fe−N1	164.31(4)	140.95(6)	152.94(12)	144.46(12)
O2−Fe−N3	92.64(4)	93.35(6)	92.26(12)	91.01(11)
O2−Fe−N5	103.37(4)	125.96(6)	115.49(13)	122.84(12)
N1−Fe−N3	81.71(4)	82.95(6)	83.07(12)	84.65(11)
N1−Fe−N5	91.31(4)	92.70(5)	91.21(12)	92.19(12)
N3−Fe−N5	89.94(4)	86.23(5)	89.83(11)	86.86(11)
τ-value ^{a}	0.094	0.607	0.327	0.554

^{a} For a definition of the τ-value, see references 41 and 42. A five-coordinate complex with ideal square-pyramidal geometry would have a τ-value of 0.0, while those with ideal trigonal bipyramidal geometry would have a value of 1.0.

coordination number. The overall geometry depends strongly on the steric properties of the acac^X ligand. Structures possessing the acac and acac^{F3} ligands are best described as distorted square-pyramids (τ = 0.09 and 0.33 for **2-acac** and **2-acac^{F3}**, respectively), whereas **2-acac^{PhF3}** and **2-acac^{tBu}** exhibit trigonal bipyramidal geometries (τ = 0.56 and 0.61, respectively) in which the O$_{acac}$ atom proximal to the bulky substituent (Ph or ^{t}Bu) occupies an axial position (Figure 1C).[41,42] The axial and equatorial Fe−O$_{acac}$ bond lengths diverge as the structure shifts toward a trigonal bipyramidal geometry. This asymmetry is also evident in the metric parameters of the acac^X ligands. For **2-acac^{tBu}**, the C3−C4 bond is 0.043(7) Å shorter than the corresponding C2−C3 bond, while the O2−C4 bond is 0.031(5) Å longer than the O1−C2 bond (similar values are observed in **2-acac^{PhF3}**). These results indicate that the negative charge of the acac ligand is primarily localized on the equatorial O-atom in structures with distorted trigonal bipyramidal geometries.

Metric data for complexes with the neutral ^{Ph}TIP ligand ([**3-acac^X**]**OTf**; acac^X = acac, acac^{F3}, acac^{F6}, and acac^{PhF3}) are provided in Table 4, and two prototypical crystallographic structures from this series are shown in Figure 2. Crystals of these triflate salts were obtained by either the slow cooling of MeCN solutions or the diffusion of pentane into CH$_2$Cl$_2$ solutions. Analysis of the crystal packing reveals that each triflate counteranion forms hydrogen bonds with three imidazole N−H groups in the solid state. In general, the [**3-acac^X**]**OTf** complexes exhibit 5C Fe(II) geometries that are intermediate between square pyramidal and trigonal bipyramidal (τ-values between 0.38 to 0.56). The lone exception is [**3-acac^{F6}(MeCN)**]**OTf**, which features a 6C Fe(II) center with a bound solvent ligand (Figure 2B). In the 5C structures, the Ph rings of the ^{Ph}TIP ligand
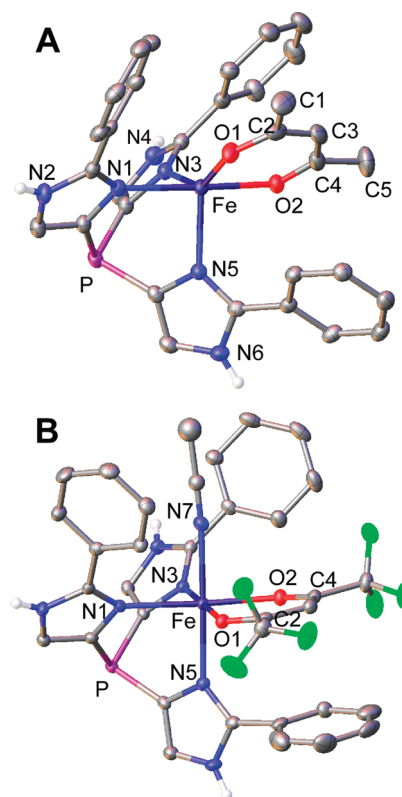
Figure 2. Thermal ellipsoid plots (50% probability) derived from [**3-acac**]**OTf**·MeCN (A) and [**3-acac^{F6}(MeCN)**]**OTf**·2MeCN (B). Noncoordinating solvent molecules, counteranions, and most hydrogen atoms have been omitted for clarity.

lie roughly parallel to the plane of the acac^X ligand, shielding the vacant coordination site. By contrast, the presence of the coordinated MeCN ligand in [**3-acac^{F6}(MeCN)**]**OTf** forces two of the Ph rings to adopt orientations perpendicular to the acac^{F6} ligand (Figure 2B).

Comparison of structures with the same coordination number and acac^X ligand indicates that Fe−N bond distances involving the neutral ^{Ph}TIP ligands are consistently longer than those involving the anionic ^{R2}Tp ligands. For example, the Fe−N$_{TIP}$ bond distances in 6C [**3-acac^{F6}(MeCN)**]**OTf** are lengthened by ∼0.08 Å (on average) relative to the Fe−N$_{Tp}$ distances in **1-acac^{F6}**. Yet this difference is less pronounced when one compares 5C complexes with the same acac^X ligand. In these cases, the Fe−N$_{TIP}$ bond distances are only ∼0.02 Å longer (on average) than the corresponding Fe−N$_{Tp}$ bond distances.

B. Spectroscopic and Electrochemical Properties. UV−vis absorption spectra of the reported Fe-acac^X complexes, measured in MeCN at room temperature, are shown in Figure 3. Along with intense near-UV peaks (not shown), two broad absorption manifolds with ε-values between 0.2 and 1.2 mM^{-1} cm^{-1} are observed in the visible region, giving the complexes their distinctive colors. These two features are separated by ∼6000−8000 cm^{-1}, although the higher-energy band is often obscured in the **2-acac^X** and [**3-acac^X**]**OTf** spectra because of the onset of Ph-based transitions in the near-UV. It is apparent in most spectra that the lower-energy band is composed of two (or more) overlapping peaks. Within each series, this feature red-shifts as the acac^X ligand becomes more electron-poor, suggesting that it primarily arises from an Fe(II)→acac^X MLCT transition—an assignment confirmed by

Table 4. Selected Bond Distances (Å) and Bond Angles (deg) for [3-acac]OTf·MeCN, [3-acac^F3]OTf·CH₂Cl₂, [3-acac^PhF3]OTF·4CH₂Cl₂, and [3-acac^F6]OTf·3MeCN

	[3-acac]	[3-acac^F3]	[3-acac^PhF3]	[3-acac^F6(MeCN)]
	OTf·MeCN	OTf·CH₂Cl₂	OTf·4CH₂Cl₂	OTf·2MeCN
Fe−O1	1.9619(12)	1.930(11)	1.974(2)	2.0792(10)
Fe−O2	2.0586(11)	2.120(11)	2.070(2)	2.0918(11)
Fe−N1	2.2122(13)	2.2225(12)	2.193(3)	2.2639(13)
Fe−N3	2.1212(13)	2.0985(13)	2.109(2)	2.1705(11)
Fe−N5	2.1376(13)	2.1289(12)	2.120(2)	2.2123(13)
Fe−N7				2.1854(14)
Fe−O_acac (ave)	2.010	2.025	2.022	2.086
Fe−N_TIP (ave)	2.157	2.151	2.141	2.216
O1−Fe−O2	87.47(5)	86.5(3)	85.96(9)	83.89(4)
O1−Fe−N1	94.46(5)	96.9(4)	95.77(9)	93.67(4)
O1−Fe−N3	142.76(5)	138.0(8)	150.09(10)	178.87(4)
O1−Fe−N5	123.96(5)	126.7(7)	114.71(9)	89.97(4)
O2−Fe−N1	176.36(5)	176.2(3)	172.64(9)	175.81(5)
O2−Fe−N3	92.12(5)	91.0(3)	89.86(9)	96.03(5)
O2−Fe−N5	90.73(5)	88.5(4)	95.87(9)	92.45(5)
N1−Fe−N3	84.47(5)	85.35(5)	85.08(10)	86.48(5)
N1−Fe−N5	90.75(5)	90.62(5)	89.92(9)	90.95(5)
N3−Fe−N5	93.28(5)	95.04(5)	95.17(9)	88.90(5)
τ-value [a]	0.560	0.637	0.376	−

[a] For a definition of the τ-value, see references 41 and 42. A five-coordinate complex with ideal square-pyramidal geometry would have a τ-value of 0.0, while those with ideal trigonal bipyramidal geometry would have a value of 1.0.
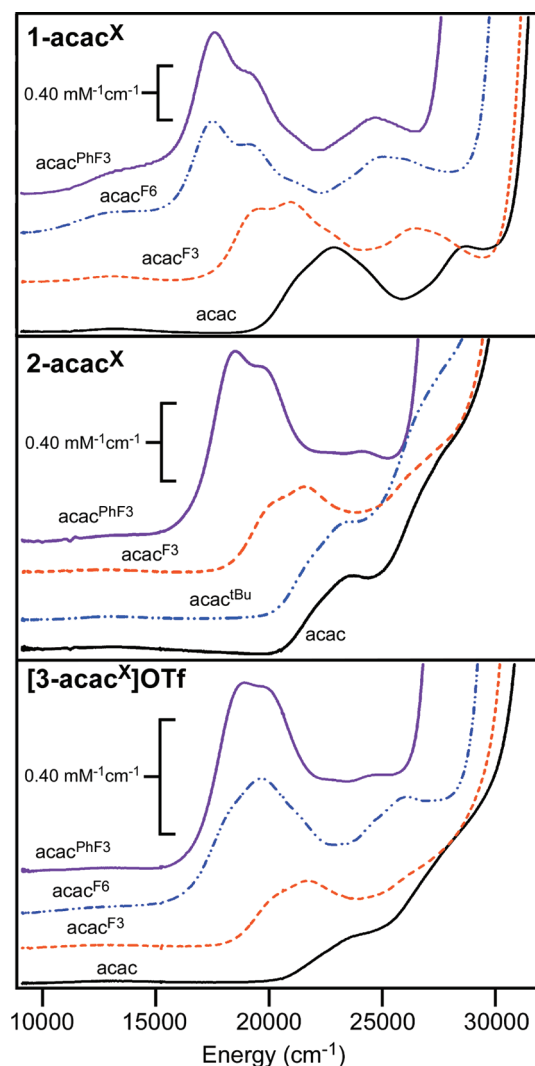

Figure 3. Electronic absorption spectra of the Fe(II)-acac complexes **1-acac^X**, **2-acac^X**, and [**3-acac^X**]**OTf** measured at room temperature in MeCN. For the **2-acac^X** complexes, a small amount (<5%) of toluene was present to enhance solubility.

literature precedents[27] and time-dependent DFT (TD-DFT) studies (vide infra). Our TD-DFT calculations further indicate that the higher-energy feature corresponds to an acac^X-based transition with some Fe(II)→acac^X MLCT character. The MLCT intensities are strongly dependent on the identity of the acac^X ligand, following the order acac^PhF3 > acac^F6 > acac^F3 > acac in each series. A complete summary of absorption energies and intensities are provided in Table 5.

It is instructive to compare absorption data for complexes with the same acac^X ligand but different supporting ligands. For instance, the MLCT bands of the ^Ph2Tp-based complexes (**2-acac^X**) are blue-shifted by 900 ± 100 cm^{-1} relative to their counterparts in spectra of the ^Me2Tp-based complexes (**1-acac^X**). Given that these species share virtually identical ligand environments, such significant disparities in absorption energies suggest that the difference in coordination number observed in the solid-state structures persists in solution. The MLCT absorption features of the ^PhTIP complexes ([**3-acac^X**]**OTf**) are higher in energy than those of the corresponding ^Me2Tp and ^Ph2Tp complexes by an average of 1400 and 250 cm^{-1}, respectively. This result indicates that the Fe(II) d-orbitals are stabilized in the ^PhTIP models relative to the Tp complexes, likely because of the difference in charge of the supporting ligands. In addition, MLCT absorption features in the [**3-acac^X**]**OTf** series are much weaker than analogous bands in the **1-acac^X** and **2-acac^X** series (Table 5), suggesting that the L_{N3} ligands also modulate Fe-acac^X covalency.

^{1}H and ^{19}F NMR spectra of the Fe-acac^X complexes were measured in MeCN-d₃ (**1-acac^X** and [**3-acac^X**]**OTf**) or benzene-d₆ (**2-acac^X**) at ambient temperature; ^{1}H spectra for **1-acac**,

2-acac, and [**3-acac**]**OTf** are shown in Figure 4. The wide range of observed chemical shifts confirms that these Fe(II) complexes possess high-spin ($S = 2$) electronic configurations. Assignments were made on the basis of chemical shifts and peak integrations, T_1-relaxation values, and literature precedents. In all cases, the three pyrazole (or imidazole) ligands are spectroscopically equivalent in solution, suggesting that the positions of the acac^X ligands are dynamically averaged on the NMR time scale.[43] ^{1}H NMR data for complexes in the **1-acac^X** and **2-acac^X** series are summarized in Supporting Information, Tables S1 and S2, respectively. The 4-pyrazole protons appear between 54 and 62 ppm, consistent with prior studies of Fe(II) species with ^R2Tp ligands. For complexes with the ^Me2Tp ligand, signals arising from the 3-Me and 5-Me pyrazole substituents are easily distinguished by their different T_1-values of 2.5 ± 0.1 and 38 ± 4 ms, respectively. In the **2-acac^X** series, the observed resonances largely conform to the pattern reported by Mehn et al. for five-coordinate (^Ph2Tp)Fe(II)(α-keto carboxylate) complexes.[21] For both sets of compounds, the *ortho* protons of the 3-Ph rings display

negative chemical shifts and remarkably short T_1-values (<1 ms), reflecting their close proximity to the paramagnetic Fe(II) center.

Each [**3-acac^X**]**OTf** complex exhibits a downfield resonance near 65 ppm with a T_1-value of 6 ± 1 ms (Table 6). This peak gradually disappears upon mixing with MeOH-d_4, indicating that it arises from the exchangeable proton of the imidazole moieties. The other intense downfield signal (found between 35 and 50 ppm) also integrates to three protons, and it is assigned to the 5-imidazole protons. On the basis of similarities to NMR spectra of the Fe(^{Ph2}Tp) complexes, we attribute the fast-relaxing peak ($T_1 \sim 1$ ms) in the negative δ-region to *ortho* protons of the 2-phenyl substituents. The corresponding *meta* and *para* protons appear near 6.5 and 7.8 ppm, respectively. ^{19}F NMR spectra of [**3-acac^X**]**OTf** complexes with fluorinated β-diketonates each display two resonances: a sharp peak at −79.2 ppm from the triflate counteranion, and a fast-relaxing feature ($T_1 = 6 \pm 3$ ms) between −45 and −65 ppm derived from the acac^X ligands. The chemical shift measured for the triflate counteranions is identical to that observed for [NBu$_4$]OTf in MeCN-d_3.[44] Interestingly, both **1-acac^{F6}** and [**3-acac^{F6}**]**OTf** exhibit only one acac^{F6}-derived resonance, indicating that the two −CF$_3$ groups are equivalent in solution because of dynamic averaging (vide supra).

Regardless of the L$_{N3}$ supporting ligands, peaks arising from methyl substituents of the acac and acac^{F3} ligands exhibit upfield chemical shifts ranging from −7 to −34 ppm. Interestingly, the T_1-values of the acac-Me resonances fall into two classes: those measured for **1-acac** and **1-acac^{F3}** are near 10 ms, while those measured for [**3-acac**]**OTf** and [**3-acac^{F3}**]**OTf** are considerably shorter (~3 ms) and close to the value found for **2-acac** in benzene-d_6 (3.3 ms). This result suggests that the acac^X ligands adopt different orientations with respect to the Fe(II) center in the two sets of complexes, and provides further evidence that complexes with bulky Ph-substituents remain pentacoordinate even in MeCN solution. In addition, the T_1-values of [**3-acac^{F6}**]**OTf**—the only 6-coordinate ^{Ph}TIP complex in the solid state—are significantly larger than those measured for the other three [**3-acac^X**]**OTf** species, indicating differences in solution structures.

The redox properties of the Fe-acac^X complexes were examined with cyclic voltammetry in MeCN solutions with (NBu$_4$)PF$_6$ as the supporting electrolyte (a 1:1 MeCN:CH$_2$Cl$_2$ mixture was used for the **2-acac^X** complexes because of their limited solubility in MeCN). The electrochemical data are summarized in Table 5 (potentials are reported vs Fc$^{+/0}$), while Figure 5 displays representative cyclic voltammograms for complexes with the acac^{PhF3} ligand. Each ^{R2}Tp complex exhibits a quasi-reversible one-electron oxidation wave corresponding to the Fe(II/III) couple. As expected, within each series the redox potentials shift to more positive values as the acac^X ligand becomes more electron-poor ($E_{acac} < E_{acac^{F3}} < E_{acac^{PhF3}} < E_{acac^{F6}}$). Potentials measured for the **2-acac^X** complexes are 210 ± 25 mV more positive than those in the **1-acac^X** series. As shown in Figure 5, the ^{Ph}TIP complex [**3-acac^{PhF3}**]**OTf** displays an anodic wave at +410 mV along with a much weaker cathodic wave at +190 mV, suggesting that the oxidation is irreversible. Such behavior is typical of the [**3-acac^X**]**OTf** complexes, and thus only the $E_{p,a}$ values are provided in Table 5 ([**3-acac^{F6}**]**OTf** failed to show any electrochemical events in the range examined). Regardless, the data clearly indicate that the [**3-acac^X**]**OTf** complexes are harder to oxidize than the corresponding ^{R2}Tp-based complexes, with $E_{p,a}$ values shifted positively by 100−200 mV relative to the **2-acac^X** series. Thus, the electrochemical results are consistent with the trend observed for Fe(II)→acac^X MLCT energies (vide supra);

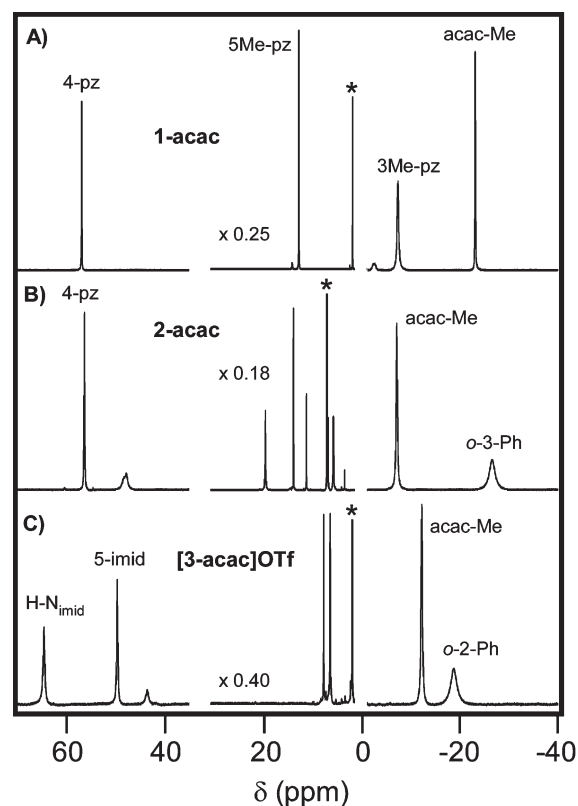**Figure 4.** ^{1}H NMR spectra of **1-acac** in MeCN-d_3 (A), **2-acac** in benzene-d_6 (B), and [**3-acac**]**OTf** in MeCN-d_3. Spectra were referenced to the residual solvent peaks (indicated by *). Note that peak intensities in the middle portions of the spectra were reduced for the sake of clarity.

both sets of data indicate the Fe(II) oxidation state is stabilized in the order ^{Ph}TIP > ^{Ph2}Tp > ^{Me2}Tp.

C. Density Functional Theory (DFT) Calculations. Energy-minimized structures of the Fe-acac^X complexes were generated via DFT geometry optimizations. On the basis of the crystallographic results, computational models of the **1-acac^X** complexes included a bound MeCN ligand, while those of the **2-acac^X** series were exclusively 5C. For the sake of comparison, structures of the [**3-acac^X**]$^+$ complexes were computed both with and without coordinated MeCN. As shown in Supporting Information, Tables S3−S5, the DFT-derived structures agree quite well with the crystallographic results, generally providing bond distances within 0.05 Å of the experimental values. Consistent with the XRD data, DFT predicts Fe−N$_{TIP}$ bond distances to be 0.103 ± 0.002 Å longer (on average) than Fe−N$_{Tp}$ distances for 6C complexes and 0.023 ± 0.002 Å longer for 5C complexes, assuming the same acac^X ligand. However, DFT uniformly overestimates all Fe−N$_{Tp/TIP}$ bond lengths by approximately 0.03 Å, regardless of L$_{N3}$ ligand, while underestimating the Fe−O$_{acac}$ by the same amount. In addition, the computed 5C models tend to exhibit larger τ-values (i.e., geometries closer to the trigonal-bipyramidal limit) than the experimental structures.

Spin-unrestricted single-point DFT calculations utilizing the B3LYP hybrid functional were performed with the optimized models. Representative molecular orbital (MO) energy-level diagrams are shown in Figure 6 for **1-acac^{F6}** and [**3-acac^{F6}(MeCN)**]$^{+}$.[45] The lone spin-down Fe electron lies in the 3d$_{xz}$-based MO that bisects the N$_{eq}$−Fe−O angles, while the highest-occupied acac-based MO

11985

dx.doi.org/10.1021/ic201115s |*Inorg. Chem.* 2011, 50, 11978−11989

Table 5. Physical Properties of Fe(II)-acac^X Complexes and Comparison to Enzymatic Systems

complex	color	UV−vis energy, cm^{-1} (ε, M^{-1} cm^{-1}) ^{a}		electrochemistry $E_{1/2}$, mV vs Fc$^{+/0}$ (ΔE, mV) ^{b}
1-acac	yellow	22830 (620)	28730 (630)	−303 (72)
1-acac^{F3}	orange	20880 (580)	26520 (400)	−34 (107)
1-acac^{PhF3}	reddish purple	17640 (1190)	24810 (570)	−2 (98)
1-acac^{F6}	purple	17510 (820)	25130 (560)	+225 (127)
2-acac	yellow	23810 (410)	28090 (sh)	−58 (133)
2-acac^{tBu}	yellow	23590 (420)	27700 (sh)	+47 (116)
2-acac^{F3}	orange	21650 (440)	27550 (sh)	+158 (91)
2-acac^{PhF3}	purple	18520 (980)	24100 (460)	+195 (94)
[3-acac]OTf	faint yellow	24090 (160)	28490 (sh)	$E_{p,a}$ = +120 ^{c}
[3-acac^{F3}]OTf	orange	21690 (220)	26810 (sh)	$E_{p,a}$ = +360 ^{c}
[3-acac^{PhF3}]OTf	reddish purple	18940 (630)	24510 (320)	$E_{p,a}$ = +410 ^{c}
[3-acac^{F6}]OTf	purple	19650 (450)	26180 (390)	N/A
Dke1-acac ^{d}		24000 (1000)	28000 (sh)	
HPPD-acac ^{d}		23000 (760)	27500 (sh)	
Dke1-acac^{F3} ^{e}		22200 (270)	26200 (280)	
Dke1-acac^{PhF3} ^{e}		18500 (350)		

^{a} sh = shoulder; no intensity is reported. ^{b} $\Delta E = E_{p,a} - E_{p,c}$ ^{c} Only the $E_{p,a}$ value is provided because of irreversibility. N/A = no electrochemical event was observed. ^{d} Data obtained from reference 27. HPPD = hydroxyphenylpyruvate dioxygenase. ^{e} Data obtained from reference 14.

exhibits a large lobe of electron density on the central carbon atom that reflects the anionic nature of the ligand (Figure 7). The spin-down lowest unoccupied MO (LUMO) has mainly acac^{F6} C=O* character, albeit with non-negligible Fe character (~7%). The Fe 3d$_{xy}$- and 3d$_{yz}$-based MOs lie at slightly higher energies. Thus, the acac LUMO orbital is approximately isoenergetic with the Fe(II) "t$_{2g}$-set" of orbitals, resulting in significant π-backbonding interactions. Similar bonding patterns were found for all 6C complexes in the **1-acac^X** and [**3-acac^X(MeCN)**]$^+$ series, although the strength of the π-backbonding interactions varied according to the electronic properties of the acac^X substituents.

The DFT results permitted further comparison of the electronic properties of the ^{R2}Tp and ^{Ph}TIP supporting ligands. Because of the difference in charge between the two sets of complexes, it was first necessary to normalize the orbital energies. This was accomplished by assuming that the acac highest occupied MO (HOMO), which is essentially nonbonding with respect to the Fe(II) center and L$_{N3}$ ligand, has identical energies in complexes with the same acac^X ligand (that is, the acac^X HOMO served as an "internal energy standard"). Following this procedure, it is evident in Figure 6 that the Fe d-orbital manifold of [**3-acac^{F6}(MeCN)**]$^+$ is uniformly stabilized relative to the corresponding set of **1-acac^{F6}** orbitals, reflecting the reduced donor strength of the neutral ^{Ph}TIP ligand compared to the anionic ^{Me2}Tp ligand. Indeed, an analysis of DFT results for the four pairs of 6C Fe-acac^X species reveals that Fe d-based MOs in ^{Ph}TIP complexes are stabilized by an average of 0.9 ± 0.3 eV relative to their counterparts in ^{Me2}Tp models. The contrast between the Tp and TIP ligands is less dramatic for the 5C complexes, where the difference in Fe d-orbital energies is only ~0.3 eV (Supporting Information, Figure S1 provides MO energy-level diagrams for 5C models of **2-acac^{F3}** and [**3-acac^{F3}**]$^+$; MO contour plots for [**3-acac^{F3}**]$^+$ are shown in Supporting Information, Figure S2).
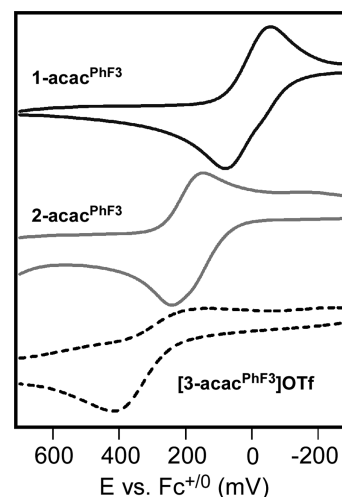
Figure 5. Cyclic voltammograms of **1-acac^{PhF3}**, **2-acac^{PhF3}**, and [**3-acac^{PhF3}**]OTf in MeCN (or 1:1 MeCN:CH$_2$Cl$_2$ for **2-acac^{PhF3}**) with 60 mM (NBu$_4$)PF$_6$ as the supporting electrolyte and a scan rate of 100 mV/s.

To aid in assignment of the observed UV−vis absorption features, TD-DFT calculations were performed for both 5C and 6C models of the [**3-acac^X**]$^+$ complexes. Regardless of coordination number, TD-DFT predicts two intense features in the visible region: a Fe(xz) → acac^X MLCT transition and a higher-energy acac^X-based transition with some MLCT character (electron density difference maps for the calculated transitions are provided in Supporting Information, Figure S3). As shown in Table 7, the computed energies for both types of transitions agree reasonably well with the experimental data. While TD-DFT consistently overestimates the MLCT intensities, it nicely reproduces the trend (observed experimentally) that these transitions weaken as the acac^X ligand becomes more

Table 6. Summary of ^{1}H NMR Parameters for $[3\text{-acac}^X]$OTf Complexes[a]

	4-imid	o-2-Ph	m-2-Ph	p-2-Ph	N−H	acac^X
				^{1}H NMR parameters		
complex	δ, ppm	δ, ppm	δ, ppm	δ, ppm	δ, ppm	δ, ppm
$[3\text{-acac}]$OTf	50 (4.0)	−19 (0.45)	6.5 (8.1)	7.8 (23)	65 (5.2)	−12 (−CH$_3$, 2.9), 44 (-H, 1.0)
$[3\text{-acac}^{F3}]$OTf	47 (4.3)	−14 (0.56)	6.4 (8.9)	7.9 (24)	66 (6.1)	−21 (−CH$_3$, 3.4), 27.2 (-H, 1.6)
$[3\text{-acac}^{PhFe}]$OTf	45 (4.5)	−13 (0.62)	6.4 (9.3)	7.8 (25)	66 (6.5)	8.0 (m-Ph, 35), 16 (p-Ph, 77), 19 (o-Ph, 2.9), 26 (-H, 1.4)
$[3\text{-acac}^{F6}]$OTf	35 (8.0)	−4.5 (1.2)	7.2 (15)	7.8 (33)	67 (7.0)	5.1 (-H, 3.3)

[a] All spectra were measured in MeCN-d_3. The numbers in parentheses are the relaxation times (T_1) in milliseconds.

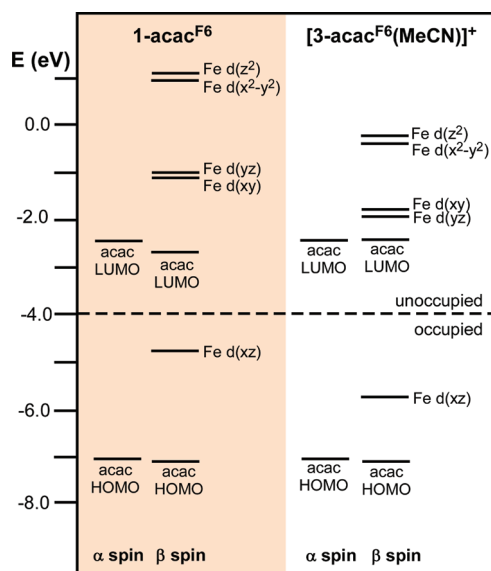**Figure 6.** MO energy diagrams for geometry-optimized models of 1-acac^{F6} and $[3\text{-acac}^{F6}(\text{MeCN})]^+$ obtained from DFT calculations. To account for differences in overall charge, the computed MO energies for $[3\text{-acac}^{F6}(\text{MeCN})]^+$ were uniformly increased by 2.11 eV, such that the acac HOMOs are isoenergetic for the two models (see text for more details).

Figure 7. Isosurface plots of spin-down MOs computed for $[3\text{-acac}^{F6}(\text{MeCN})]^+$ by DFT.

Table 7. Comparison of Experimental and TD-DFT Computed Transition Energies

		MLCT		acac^X-based	
		E, cm^{-1}	ε, mM^{-1} cm^{-1a}	E, cm^{-1}	ε, mM^{-1} cm^{-1a}
$[3\text{-acac}]^+$	6C DFT	25363	0.90	25363	0.07
	5C DFT	26130	0.60	26130	0.14
	exp	24090	0.16	28490	N/A
$[3\text{-acac}^{F3}]^+$	6C DFT	22597	1.50	23683	0.03
	5C DFT	23542	0.39	25842	0.11
	exp	21690	0.22	26810	N/A
$[3\text{-acac}^{PhF3}]^+$	6C DFT	20036	2.27	22139	0.27
	5C DFT	20244	1.02	22873	0.83
	exp	18940	0.63	24510	0.32
$[3\text{-acac}^{F6}]^+$	6C DFT	19834	2.02	22093	0.01
	5C DFT	18830	1.18	22406	0.17
	exp	19650	0.45	26180	0.39

[a] Assumed $\nu_{1/2}$-value of 2500 cm^{-1}.

electron rich. The MLCT transitions are most intense for the 6C complexes, since overlap between the donor Fe(xz) orbital and the acceptor acac^X LUMO is maximized when the acac^X ligand lies in the equatorial plane. As the geometry shifts toward trigonal bipyramidal in the 5C complexes, this orbital overlap is reduced. In addition, intermediate τ-values facilitate mixing between the MLCT and acac^X-based transitions, thereby increasing the intensity of the latter at the expense of the former in 5C complexes.

4. SUMMARY AND IMPLICATIONS FOR DKE1

This Paper has described the synthesis of three series of Fe(II) β-diketonato complexes designed to model the acac-bound form of Dke1 and replicate variations in the facial triad (2H1C vs 3His) found in nonheme Fe dioxygenases. Adjustment of the steric properties of the Tp ligands resulted in the formation of both 5C and 6C complexes, and β-diketonato ligands with a range of steric and electronic properties were employed to aid in the interpretation of results. Each complex was extensively characterized with experimental and computational methods, including X-ray crystallography, UV−vis and NMR spectroscopies, CV, and DFT calculations. Thus, the 12 reported
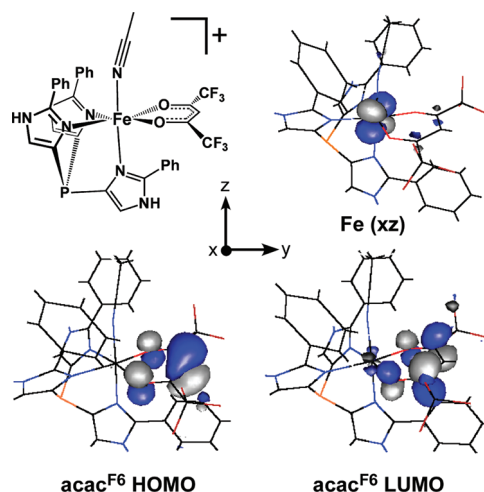
complexes have permitted a *systematic examination* of the roles of the L$_{N3}$ and acac^X ligands in determining the structural, spectroscopic, electrochemical, and electronic properties of the Fe(II) models. Comparison of complexes featuring anionic (^{R2}Tp) and neutral (^{Ph}TIP) supporting ligands, but identical acac^X ligands, reveals the following key differences: (i) regardless of coordination

number, Fe–N_{TIP} bond distances are consistently longer than Fe–N_{Tp} distances (Tables 2–4), (ii) the Fe(II)→$acac^X$ MLCT features appear at higher energies for the ^{Ph}TIP complexes (Figure 3; Table 5), and (iii) redox potentials of the ^{R2}Tp complexes are more negative than those of the corresponding ^{Ph}TIP complexes (Figure 5; Table 5). DFT calculations further confirm that the ^{Ph}TIP ligand is a significantly weaker donor, as seen in the relative stabilization of the Fe d-orbitals (Figure 6). We will now discuss the relevance of these findings for the electronic structure of the Dke1 active site.

Diebold et al. recently published a study in which the spectroscopic features of acac-bound Dke1 were compared with those of acac-bound hydroxyphenylpyruvate dioxygenase (HPPD), an enzyme that possesses the conventional 2H1C facial triad.[27] Prior to that, Straganz and Nidetzky reported the absorption spectra of Dke1 coordinated to various β-diketonates.[14] Like our models, substrate-bound Dke1 exhibits an intense near-UV band and two broad features in the visible region with ε-values between 0.2 and 1.0 $mM^{-1} cm^{-1}$ (Table 5). Diebold et al. also used CD and MCD spectroscopies to observe much weaker ligand-field transitions at lower energies. Analysis of these ligand-field bands revealed only minor differences between enzymes with the 3His and 2H1C triads; however, the MLCT feature is shifted to lower energy by ~1000 cm^{-1} in the 2H1C system. Similarly, for our synthetic $[(L_{N3})Fe^{2+}(acac^X)]^{0/+}$ complexes, the absorption features of the 1-$acac^X$ series are red-shifted by an average of 1400 cm^{-1} relative to the $[3$-$acac^X]OTf$ series. In general, the 5C 2-$acac^X$ and $[3$-$acac^X]OTf$ spectra exhibit excellent agreement with the Dke1-$acac^X$ absorption data, while the 6C 1-$acac$ spectrum is nearly identical to the one reported for HPPD-acac.[27] Thus, while our results indicate that the ^{Ph}TIP ligand accurately reproduces the enzymatic 3His coordination environment, they would also seem to corroborate the conclusion of Diebold et al. that variations in the facial triad give rise to only modest spectral perturbations.

Yet analysis of the electronic transitions may not provide a complete picture. Our electrochemical results indicate that the $[3$-$acac^X]OTf$ complexes are harder to oxidize than the corresponding 2-$acac^X$ complexes by an average of 145 mV, even though the two sets exhibit similar absorption energies. Thus, the charge of the supporting ligands has a significant impact on the redox potential of the Fe center—a crucial parameter in tuning the O_2 reactivity of the Fe-$acac^X$ unit. These experimental results are consistent with DFT calculations that indicate a sizable stabilization of the Fe d-orbital manifold in the ^{Ph}TIP complexes relative to the ^{Ph2}Tp complexes (vide supra). Of course, the Fe redox potential is somewhat irrelevant if the catalytic cycle proceeds via direct reaction of O_2 with the bound acac ligand, a possibility suggested by Straganz and Nidetzky;[14] our results, however, cast some doubts on this scenario. First, the proposed mechanism would require significant spin delocalization from the Fe center to the $acac^X$ ligand to overcome the spin-forbidden nature of concerted reaction with O_2. While such a scenario has been shown to occur in Fe^{3+}-containing intradiol catechol dioxygenases,[17] our DFT calculations indicate that only a small amount of unpaired spin-density resides on the $acac^X$ ligands in our models. Second, the highest-occupied MO of the coordinated acac ligand, which would play a central role in the electrophilic attack of O_2, is at least 1.0 eV lower in energy than the Fe-based MOs in all DFT models.[46] Even for complexes with electron-rich acac ligands, the frontier MOs are exclusively Fe-based, suggesting that reaction with O_2 is more likely at Fe than the ligand. This conclusion has

been confirmed experimentally in our laboratory via O_2 reactivity studies, which will be described in a future paper. Regardless, further biochemical and synthetic studies are required to fully understand the significance of the 3His triad for enzymatic function.

■ ASSOCIATED CONTENT

ⓢ Supporting Information. ^{1}H NMR data for 1-$acac^X$ and 2-$acac^X$ complexes, metric parameters for DFT-optimized models, MO energy-level diagrams for 2-$acac^{F3}$ and $[3$-$acac^{F3}]^+$, electron-density difference maps from TD-DFT calculations, and crystallographic data in CIF format. This material is available free of charge via the Internet at http://pubs.acs.org.

■ AUTHOR INFORMATION

Corresponding Author
*E-mail: adam.fiedler@marquette.edu.

■ ACKNOWLEDGMENT

■ REFERENCES

(1) (a) Parales, R. E.; Haddock, J. D. *Curr. Opin. Biotechnol.* **2004**, *15*, 374–379.(b) Wackett, L. P.; Hershberger, C. D. *Biocatalysis and Biodegradation: Microbial Transformation of Organic Compounds*; ASM Press: Washington, D.C., 2001. (c) Singh, A.; Ward, O. P. In *Biodegradation and Bioremediation*; Singh, A., Ward, O. P., Eds.; Springer: Heidelberg, Germany, 2004, pp 1–18.

(2) (a) Gibson, D. T.; Parales, R. E. *Curr. Opin. Biotechnol.* **2000**, *11*, 236–243.(b) Parales, R.; Resnick, S. M. In *Biodegradation and Bioremediation*; Singh, A., Ward, O. P., Eds.; Springer: Heidelberg, Germany, 2004, pp 175–196. (c) Costas, M.; Mehn, M. P.; Jensen, M. P.; Que, L., Jr. *Chem. Rev.* **2004**, *104*, 939–986.

(3) (a) Kauppi, B.; Lee, K.; Carredano, E.; Parales, R. E.; Gibson, D. T.; Eklund, H.; Ramaswamy, S. *Structure* **1998**, *6*, 571–586. (b) Karlsson, A.; Parales, J. V.; Parales, R. E.; Gibson, D. T.; Eklund, H.; Ramaswamy, S. *Science* **2003**, *299*, 1039–1042.

(4) (a) Han, S.; Eltis, L. D.; Timmis, K. N.; Muchmore, S. W.; Bolin, J. T. *Science* **1995**, *270*, 976–980. (b) Vaillancourt, F. H.; Bolin, J. T.; Eltis, L. D. *Crit. Rev. Biochem. Mol.* **2006**, *41*, 241–267. (c) Kovaleva, E. G.; Lipscomb, J. D. *Science* **2007**, *316*, 453–457.

(5) (a) Xun, L. Y.; Bohuslavek, J.; Cai, M. A. *Biochem. Biophys. Res. Commun.* **1999**, *266*, 322–325. (b) Xu, L.; Resing, K.; Lawson, S. L.; Babbitt, P. C.; Copley, S. D. *Biochemistry* **1999**, *38*, 7659–7669. (c) Nagata, Y.; Endo, R.; Ito, M.; Ohtsubo, Y.; Tsuda, M. *Appl. Microbiol. Biotechnol.* **2007**, *76*, 741–752.

(6) Koehntop, K. D.; Emerson, J. P.; Que, L., Jr. *J. Biol. Inorg. Chem.* **2005**, *10*, 87–93.

(7) Bruijnincx, P. C. A.; Lutz, M.; Spek, A. L.; Hagen, W. R.; Weckhuysen, B. M.; vanKoten, G.; Gebbink, R. J. M. K. *J. Am. Chem. Soc.* **2007**, *129*, 2275–2286.

(8) (a) Kovaleva, E. G.; Lipscomb, J. D. *Nature Chem. Biol.* **2008**, *4*, 186–193. (b) Lipscomb, J. D. *Curr. Opin. Struct. Biol.* **2008**, *18*, 644–649.

(9) (a) Straganz, G. D.; Nidetzky, B. *ChemBioChem* **2006**, *7*, 1536–1548. (b) Leitgeb, S.; Nidetzky, B. *Biochem. Soc. Trans.* **2008**, *36*, 1180–1186.

(10) (a) Joseph, C. A.; Maroney, M. J. *Chem. Commun.* **2007**, 3338–3349. (b) Pierce, B. S.; Gardner, J. D.; Bailey, L. J.; Brunold, T. C.; Fox, B. G. *Biochemistry* **2007**, *46*, 8569–8578.

(11) (a) Chen, J.; Li, W.; Wang, M. Z.; Zhu, G. Y.; Liu, D. Q.; Sun, F.; Hao, N.; Li, X. M.; Rao, Z. H.; Zhang, X. C. *Protein Sci.* **2008**, *17*, 1362–1373. (b) Matera, I.; Ferraroni, M.; Burger, S.; Scozzafava, A.; Stolz, A.; Briganti, F. *J. Mol. Biol.* **2008**, *380*, 856–868. (c) Hintner, J. P.; Remtsma, T.; Stolz, A. *J. Biol. Chem.* **2004**, *279*, 37250–37260.

(12) Straganz, G. D.; Glieder, A.; Brecker, L.; Ribbons, D. W.; Steiner, W. *Biochem. J.* **2003**, *369*, 573–581.

(13) Straganz, G. D.; Hofer, H.; Steiner, W.; Nidetzky, B. *J. Am. Chem. Soc.* **2004**, *126*, 12202–12203.

(14) Straganz, G. D.; Nidetzky, B. *J. Am. Chem. Soc.* **2005**, *127*, 12306–12314.

(15) (a) Straganz, G. D.; Diebold, A. R.; Egger, S.; Nidetzky, B.; Solomon, E. I. *Biochemistry* **2010**, *49*, 996–1004. (b) Diebold, A. R.; Straganz, G.; Solomon, E. I. *J. Amer. Chem.* **2011**, *113*, 15979–15991.

(16) Leitgeb, S.; Straganz, G. D.; Nidetzky, B. *Biochem. J.* **2009**, *418*, 403–411.

(17) (a) Pau, M. Y. M.; Davis, M. I.; Orville, A. M.; Lipscomb, J. D.; Solomon, E. I. *J. Am. Chem. Soc.* **2007**, *129*, 1944–1958. (b) Pau, M. Y. M.; Lipscomb, J. D.; Solomon, E. I. *Proc. Natl. Acad. Sci. U.S.A.* **2007**, *104*, 18355–18362.

(18) Siewert, I.; Limberg, C. *Angew. Chem., Int. Ed.* **2008**, *47*, 7953–7956.

(19) Kitajima, N.; Amagai, H.; Tamura, N.; Ito, M.; Morooka, Y.; Heerwegh, K.; Penicaud, A.; Mathur, R.; Reed, C. A.; Boyd, P. D. W. *Inorg. Chem.* **1993**, *32*, 3583–3584.

(20) (a) Ogihara, T.; Hikichi, S.; Akita, M.; Moro-oka, Y. *Inorg. Chem.* **1998**, *37*, 2614–2615. (b) Mukherjee, A.; Cranswick, M. A.; Chakrabarti, M.; Paine, T. K.; Fujisawa, K.; Munck, E.; Que, L. *Inorg. Chem.* **2010**, *49*, 3618–3628. (c) Paine, T. K.; Zheng, H.; Que, L., Jr. *Inorg. Chem.* **2005**, *44*, 474–476.

(21) Mehn, M. P.; Fujisawa, K.; Hegg, E. L.; Que, L., Jr. *J. Am. Chem. Soc.* **2003**, *125*, 7828–7842.

(22) (a) Brown, R. S.; Huguet, J. *Can. J. Chem.* **1980**, *58*, 889–901. (b) Breslow, R.; Hunt, J. T.; Smiley, R.; Tarnowski, T. *J. Am. Chem. Soc.* **1983**, *105*, 5337–5342. (c) Slebocka-Tilk, H.; Cocho, J. L.; Frakman, Z.; Brown, R. S. *J. Am. Chem. Soc.* **1984**, *106*, 2421–2431. (d) Allen, W. E.; Sorrell, T. N. *Inorg. Chem.* **1997**, *36*, 1732–1734. (e) Kimblin, C.; Allen, W. E.; Parkin, G. *J. Chem. Soc., Chem. Commun.* **1995**, 1813–1815. (f) Lynch, W. E.; D. M. Kurtz, J.; Wang, S.; Scott, R. A. *J. Am. Chem. Soc.* **1994**, *116*, 11030–11038. (g) Kunz, P. C.; Reiss, G. J.; Frank, W.; Klaui, W. *Eur. J. Inorg. Chem.* **2003**, 3945–3951.

(23) Kunz, P. C.; Klaui, W. *Collect. Czech. Chem. Commun.* **2007**, *72*, 492–502.

(24) (a) Malkhasian, A. Y. S.; Nikolovski, B.; Kucera, B. E.; Loloee, R.; Chavez, F. A. Z. *Anorg. Allg. Chem.* **2007**, *633*, 1000–1005. (b) Batten, M. P.; Canty, A. J.; Cavell, K. J.; Ruther, T.; Skelton, B. W.; White, A. H. *Acta. Crystallogr., Sect. C* **2004**, *60*, M311–M313.

(25) Wu, F. J.; Kurtz, D. M. *J. Am. Chem. Soc.* **1989**, *111*, 6563–6572.

(26) (a) Wu, F. J.; Kurtz, D. M.; Hagen, K. S.; Nyman, P. D.; Debrunner, P. G.; Vankai, V. A. *Inorg. Chem.* **1990**, *29*, 5174–5183. (b) Vankai, V. A.; Newton, M. G.; Kurtz, D., Jr. *Inorg. Chem.* **1992**, *31*, 342–343.

(27) Diebold, A. R.; Neidig, M. L.; Moran, G. R.; Straganz, G. D.; Solomon, E. I. *Biochemistry* **2010**, *49*, 6945–6952.

(28) Malbosc, F.; Chauby, V.; Serra-Le Berre, C.; Etienne, M.; Daran, J. C.; Kalck, P. *Eur. J. Inorg. Chem.* **2001**, 2689–2697.

(29) Kitajima, N.; Fujisawa, L.; Fujimoto, C.; Moro-oka, Y.; Hashimoto, S.; Kitagawa, T.; Toriumi, K.; Tatsumi, K.; Nakamura, A. *J. Am. Chem. Soc.* **1992**, *114*, 1277–1291.

(30) Sheldrick, G. M. *Acta. Crystallogr., Sect. A* **2008**, *64*, 112–122.

(31) Dolomanov, O. V.; Bourhis, L. J.; Gildea, R. J.; Howard, J. A. K.; Puschmann, H. *J. Appl. Crystallogr.* **2009**, *42*, 339–341.

(32) Neese, F. *ORCA - an ab initio, Density Functional and Semi-empirical Program Package*, version 2.7; University of Bonn: Bonn, Germany, 2009.

(33) (a) Becke, A. D. *J. Chem. Phys.* **1986**, *84*, 4524–4529. (b) Perdew, J. P. *Phys. Rev. B* **1986**, *33*, 8822–8824.

(34) (a) Schafer, A.; Horn, H.; Ahlrichs, R. *J. Chem. Phys.* **1992**, *97*, 2571–2577. (b) Schafer, A.; Huber, C.; Ahlrichs, R. *J. Chem. Phys.* **1994**, *100*, 5829–5835.

(35) (a) Becke, A. D. *J. Chem. Phys.* **1993**, *98*, 5648–5652. (b) Becke, A. D. *J. Chem. Phys.* **1993**, *98*, 1372–1377. (c) Lee, C. T.; Yang, W. T.; Parr, R. G. *Phys. Rev. B* **1988**, *37*, 785–789.

(36) (a) Stratmann, R. E.; Scuseria, G. E.; Frisch, M. J. *J. Chem. Phys.* **1998**, *109*, 8218–8224. (b) Casida, M. E.; Jamorski, C.; Casida, K. C.; Salahub, D. R. *J. Chem. Phys.* **1998**, *108*, 4439–4449. (c) Bauernschmitt, R.; Ahlrichs, R. *Chem. Phys. Lett.* **1996**, *256*, 454–464.

(37) (a) Hirata, S.; Head-Gordon, M. *Chem. Phys. Lett.* **1999**, *314*, 291–299. (b) Hirata, S.; Head-Gordon, M. *Chem. Phys. Lett.* **1999**, *302*, 375–382.

(38) Laaksonen, L. *J. Mol. Graphics* **1992**, *10*, 33–34.

(39) In the crystal structures of **1-acac^{F3}** and [**3-acac^{F3}**]**OTf**, the acac^{F3} ligand is disordered because of interchange of the -CF$_3$ and -CH$_3$ groups. This disorder is fairly minor for **1-acac^{F3}**, as the two species exist in a 9:1 ratio; however, the problem is more severe for [**3-acac^{F3}**]**OTf**, where the relative occupancies are ∼2:1. Hence, uncertainties in bond lengths and angles are greater for the latter structure. The metric parameters reported in Tables 2 and 4 refer to the high-occupancy species.

(40) (a) Reger, D. L.; Gardinier, J. R.; Elgin, J. D.; Smith, M. D.; Hautot, D.; Long, G. J.; Grandjean, F. *Inorg. Chem.* **2006**, *45*, 8862–8875. (b) Reger, D. L.; Elgin, J. D.; Smith, M. D.; Grandjean, F.; Rebbouh, L.; Long, G. J. *Polyhedron* **2006**, *25*, 2616–2622. (c) Calogero, S.; Lobbia, G. G.; Cecchi, P.; Valle, G.; Friedl, J. *Polyhedron* **1994**, *13*, 87–97. (d) Oliver, J. D.; Mullica, D. F.; Hutchinson, B. B.; Milligan, W. O. *Inorg. Chem.* **1980**, *19*, 165–169.

(41) The geometric parameter τ is defined as $\tau = |(\alpha - \beta)|/60$, where α and β are the two basal angles in pseudo-square pyramidal geometry (see ref 42). The τ-value is 0.0 in idealized square-planar geometries and 1.0 in idealized trigonal bipyramidal geometries.

(42) Addison, A. W.; Rao, T. N.; Reedijk, J.; Vanrijn, J.; Verschoor, G. C. *J. Chem. Soc., Dalton Trans.* **1984**, 1349–1356.

(43) Equivalency between the pyrazole ligands was also found in ^{1}H NMR studies of five-coordinate (^{Ph2}Tp)Fe(II)(α-keto carboxylate) complexes. See ref 21.

(44) T_1-values for triflate anions in the [**3-acac^X**]**OTf** series were found to lie near 0.5 s, which is shorter than the value of 4 s measured for [NBu$_4$]OTf. This result suggests that the triflate anions are weakly associated with the [Fe(^{Ph}TIP)(acac^X)]$^+$ units in solution.

(45) Spin-polarization lowers the energies of the spin-up (α) Fe d orbitals relative to their spin-down (β) counterparts, resulting in substantial mixing of the former with ligand-based orbitals. For this reason, only the spin-down Fe d-based MOs are shown in Figure 6.

(46) The gap between the acac HOMO and Fe d-orbital energies is the smallest for the 5C model of [**3-acac**]$^+$, since the acac ligand is electron rich and the Fe-d-orbitals are relatively stabilized by the ^{Ph}TIP ligand and 5C environment.